Coupled terahertz quantum cascade wire lasers

Marie C. Ertl ✉ ⓘ ; Michael Jaidl ⓘ ; Benedikt Limbacher ⓘ ; Dominik Theiner ⓘ ; Miriam Giparakis ⓘ ;
Stefania Isceri ⓘ ; Maximilian Beiser ⓘ ; Aaron Maxwell Andrews ⓘ ; Gottfried Strasser ⓘ ; Juraj Darmo ⓘ ;
Karl Unterrainer ⓘ

Check for updates

View Online

Export Citation

Coupled terahertz quantum cascade wire lasers

Marie C. Ertl,[1,a] [ID] Michael Jaidl,[1] [ID] Benedikt Limbacher,[1] [ID] Dominik Theiner,[1] [ID] Miriam Giparakis,[2] [ID]
Stefania Isceri,[2] [ID] Maximilian Beiser,[2] [ID] Aaron Maxwell Andrews,[2] [ID] Gottfried Strasser,[2,3] [ID] Juraj Darmo,[1] [ID]
and Karl Unterrainer[1,3] [ID]

AFFILIATIONS

[1]Photonics Institute, TU Wien, 1040 Vienna, Austria
[2]Institute of Solid State Electronics, TU Wien, 1040 Vienna, Austria
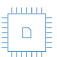[3]Center for Micro- and Nanostructures, TU Wien, 1040 Vienna, Austria

[a]Author to whom correspondence should be addressed: marie.christine.ertl@tuwien.ac.at

ABSTRACT

We present mutual optical coupling in terahertz (THz) quantum cascade wire laser arrays that are flip-chip bonded to a dielectric substrate. The mounting substrate is patterned for individual electrical contacting of each wire laser of the array. The resulting sandwich-like structure supports wire laser modes with a significant part propagating outside the cavity and mediates the long range coupling. The evanescent field part of the modes couples to the adjoining ridge, which, in turn, leads to mutual optical injection-locking between them. We demonstrate this effect for both geometrically similar and dissimilar wire lasers when biased in pulsed operation with temporally overlapping bias pulses. Finite element simulations confirm our measurement results. By applying time-shifted bias pulses to individual array elements, a controllable optical injection seeding of the wire cavity is achieved. We observe intensity modification of the laser modes with changing bias pulse overlap as a result of the injection locking. By choosing both the physical spacing of the laser ridges and the intensity of the seeding laser correctly, the relative intensities of the favored lasing modes are enhanced up to 95 percent. Understanding the coupling in THz wire laser arrays is important for future device improvements in terms of higher continuous-wave operating temperatures through better thermal dissipation, and higher output power and an improved far field due to controlled coupling of their modes.

Wire lasers[1,2] have transversal dimensions smaller than their emission wavelength, which forces a significant amount of the mode to propagate outside the laser cavity along the entire resonator length. Quantum cascade wire lasers (QCWLs) in the THz region are achievable with standard processing techniques,[3–6] harnessing the fact that quantum cascade lasers (QCLs) in the double-metal configuration already are subwavelength devices in the vertical direction.[7]

In wire lasers, a significant fraction of the optical mode intensity is outside the active waveguide, which can be exploited to modify the radiation properties of the laser. Controlling and changing the emission wavelength is advantageous for many applications, including multicolor sources,[8] imaging,[9] and spectroscopy.[10] A number of significant developments have been achieved by incorporating passive components alongside the laser cavity. These include tunability[11–13] of wire lasers, mode selection with monolithically integrated selectors,[14] antenna-[15] and π-coupling[16] schemes, and coupled arrays.[17] In many of these THz QCWL devices, elaborate device geometries have been used, enabling surface emission and electrical contacting.

Since the transversal dimension for these lasers around frequencies of 3.9 THz is in the range of 10 μm, direct wire-bonding onto the top metal contact of the laser is challenging, as the diameter of standard bond-wires is around 25 μm, making it significantly wider than the laser waveguide width. Planarizing techniques, with a low-loss polymer,[18–20] have been employed to overcome the difficulties making electrical contacts. Although the THz radiation losses in the polymer are relatively small, they are not negligible, thus making the study of coupling to adjacent devices with a significant spatial separation (several tens of micrometers) challenging. Coupled lasers have been demonstrated by various mechanisms, including diffraction wave coupling in a Talbot cavity,[21] y-coupling by connecting two ridges to one single mode waveguide,[22,23] leaky-wave coupling through laterally propagating waves,[24] mutual antenna coupling via the radiation field,[17] π-coupling through strong lateral field distribution,[16] via the common metallic ground contact of two QCLs for on-chip detection,[25] and evanescent-wave coupling via exponentially decaying fields outside the high refractive index dielectric cores of the cavities.[26]

23 September 2024 07:57:55

In this work, we present coupled THz QCWLs that can be mutually injection-lock via optical modes of different wire lasers. The array of double-metal QCWLs is bonded episide-down onto a semi-insulating GaAs (SI-GaAs) chip for electrical contacting without the need for bonding pads. We utilize the recently demonstrated episide-down flip-chip bonding technique used to contact ultrathin double-metal THz QCL ring lasers.[27] Its advantages include facilitated electrical contacting, on-chip integration, individual electrical control of each wire laser, and improved thermal management (see the supplementary material). This leads to reduced threshold current densities and improved maximum operating temperatures in continuous-wave operation. The die-bonded devices have a sandwich-like structure [Fig. 1(a)] creating a waveguide between the individual laser ridges. It is defined by the SI-GaAs substrate with metallic contacting lines on the bottom and metal (Au) on the top. The evanescent field component of the guided mode is extended between the laser cavities and facilitates the coupling of the simultaneously biased lasers. Finite element simulations show that part of this extended evanescent field couples to the underlying substrate, enabling long range coupling. The lasers injection-lock when they are operated in pulsed operation with temporally overlapping bias pulses. In the injection-lock configuration, we observe that specific modes are enhanced while others are attenuated.

The QCWLs are fabricated from a GaAs/AlGaAs heterostructure active region supporting two lasing transitions at 3.3 and 3.9 THz. The design is based on the dual-color, three-well, single stack, longitudinal optical (LO)–phonon depopulation design.[28] It contains 333 periods and has a total thickness of 15 μm. We process the active region into chiplets containing seven 1.5 mm long double-metal QCL ridges, with widths of 40/30/20/12/15/25/30 μm. Several devices were processed with spacings increasing from 38 to 150 μm, corresponding roughly to multiples of the free-space wavelength (76 μm). In addition, symmetric chiplets were fabricated with widths of 30/10/10/10/10/10/30 μm and a spacing of 76 μm. The wider ridges provide bonding stability, reference points for measurements, and additional heat sink connections (Fig. 1).

Due to the narrow width of the ridges, direct wire-bonding is not possible. Therefore, the laser chiplets are bonded episide-down onto a SI-GaAs chip with predefined Ti/Au (10/500 nm) contact lines with a sub-micron die bonder. The contact stripes are 6 μm wider than the corresponding wire lasers to facilitate the alignment and bonding. The nominal alignment accuracy of the die bonding is 1 μm. Figure 1(a) sketches the die-bonding process steps schematically. First, the finished laser die is cleaved, and the contact lines are defined on the bottom chip. In the second step, the top and bottom die are aligned with the help of a microscope and a beam splitter, contained in the die-bonding machine. Figure 1(b) shows a microscope picture of the aligned chiplets. Finally, the top chiplet is lowered onto the bottom chiplet. The chiplets are pressed together with a bonding force of 10 N and then heated to 380 °C for about 10 min, which fuses the chiplets together. The episide-down bonded laser ridges are then electrically contacted via bond-wires, placed on the protruding metal contact lines of the bottom chip [Fig. 1(c)]. The finished devices are indium soldered to a copper plate, which is mounted onto the cold finger of a helium flow cryostat. The radiation is collected by a parabolic mirror and guided into a Fourier transform infrared spectrometer (FTIR). The measured spectra have a resolution of 2.25 GHz.

The measurement setup consists of a function generator (FG) with two time-synchronized channels. It triggers the output pulses from two identical pulse generators. The timing is controlled via the FG, which triggers the bias pulses that power the lasers. Precise timing control (timing jitter < 5 ns) allows us to study the influence of the temporal bias pulse overlap on the inter-element coupling. A schematic of the setup is depicted in Fig. 1(d). The measurements were conducted in pulsed operation (0.5% duty-cycle at 10 kHz) at 5 K. For the 10 μm devices, only the duty-cycle was changed to 1% by increasing the repetition rate to 20 kHz. A reference spectrum of each individual device is measured. The lasers are then biased by the two pulse generators in time-synchronized operation.

The episide-down bonded wire laser devices are mechanically robust, and we have been able to bias up to seven electrically connected devices simultaneously in pulsed operation. Through power-current-voltage (PIV) characterization (see the supplementary material) of individual lasers, we observe significant performance improvements,
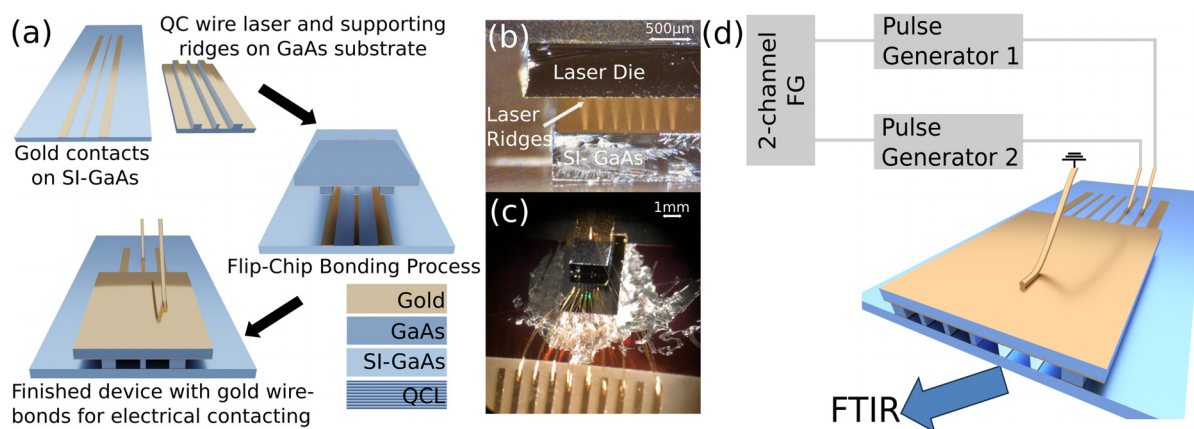
FIG. 1. (a) The schematic workflow of the episide-down bonding process. The ultrathin wire QCWLs and the gold contacts on the bottom substrate are aligned and then bonded. The microscope picture in (b) shows a side view of the aligned chiplets just before the bonding step. The finished wire-bonded device is shown in (c). (d) A schematic of the measurement setup, featuring a two-channel function generator (FG), two pulse generators, and how they are connected to the lasers. The lasing spectra are measured with a Fourier transform infrared spectrometer (FTIR).

resulting in a reduction in threshold current density up to 50% compared to a standard episide-up mounted QCL ridge with the same resonator length. The narrowest bonded devices also operate in continuous-wave mode up to 35 K. This is noteworthy given that this type of active region, designed to operate at high temperatures, is typically not capable of continuous-wave operation.

In Fig. 2, we show measured spectra of the 150 μm spaced device. The individual spectra of the 12 and 15 μm wide ridges are shown in cyan and pink, respectively [Figs. 2(a) and 2(b)]. When biasing both laser ridges simultaneously, the resulting combined spectrum intensities $I_{(A+B)}$ are not only the sum of the individually measured spectral intensities $I_A + I_B$, but also we observe that specific modes are enhanced, while others are attenuated. We quantify these spectral changes by calculating injection-induced differential spectra ΔI_{AB} [Eq. (1)], which determine the relative changes of the mode intensities in the combined spectrum compared to the sum of the single spectra [Figs. 2(c) and 2(d)]. This allows us to qualitatively compare multiple measured devices,

$$\Delta I_{AB} = \frac{I_{(A+B)}}{I_A + I_B} - 1. \tag{1}$$

The lasers injection-lock when the bias pulse timing overlaps. In this case, the simultaneously operating laser elements couple to each other, and ΔI_{AB} of Eq. (1) is non-zero. When we introduce a time delay (t_d) between the bias pulse of the seeding laser and the bias pulse

FIG. 2. The spectral evolution of an injected wire laser pair consisting of a 12 and 15 μm wide ridge. The measured lasing spectra of the single ridges at device voltages of 24.3 and 24.5 V (cyan and pink, respectively), and the combined spectrum (blue) is depicted in (a) and (b) for a bias pulse overlap (BPO) of 100%. Injection-induced differential spectra ΔI_{AB} (c) and (d) quantify the change of the combined spectrum vs the sum of the single spectra. The contour plots (e) and (f) detail the spectral changes for decreasing bias pulse overlap for two injection scenarios by visualizing the relative spectral differences. In (a), (c), and (e), the 12 μm ridge is the seeding partner vs (b), (d), and (f) where the 15 μm ridge is the seed. Red areas indicate enhanced modes, and blue areas indicate attenuated modes. The change of the BPO in percent is shown as an inset in (e).

of the second element, we observe that the affected modes change. For decreasing bias pulse overlap, previously enhanced modes become attenuated while attenuated modes experience enhancement. We measured combined spectra for the time delays indicated in the inset of Fig. 2(e) (step size 50 ns), with temporal overlap of the bias pulses given in percent. We calculate the relative intensity change via injection-induced differential spectra for each case and visualize them in contour plots [Figs. 2(e) and 2(f)]. As long as the time delay is smaller than the bias pulse width (τ_p) $0 < t_d < \tau_p$, the injection-locking stays active. We performed measurements where each of the two lasers works as the seed for the injection-locking; the seeding laser is the one that is turned on first. When the 12 μm wide QCL acts as the seed (Fig. 2, left), the coupling is stronger than when the 15 μm wide laser seeds (Fig. 2, right).

As soon as the time delay of the bias pulse exceeds the bias pulse width $t_d > \tau_p$, the measured combined spectrum becomes equal to the sum of the single spectra, and the cross term of Eq. (1) equals approximately zero. Small spectral residuals are measured due to electrical pickups between the biased lasers.
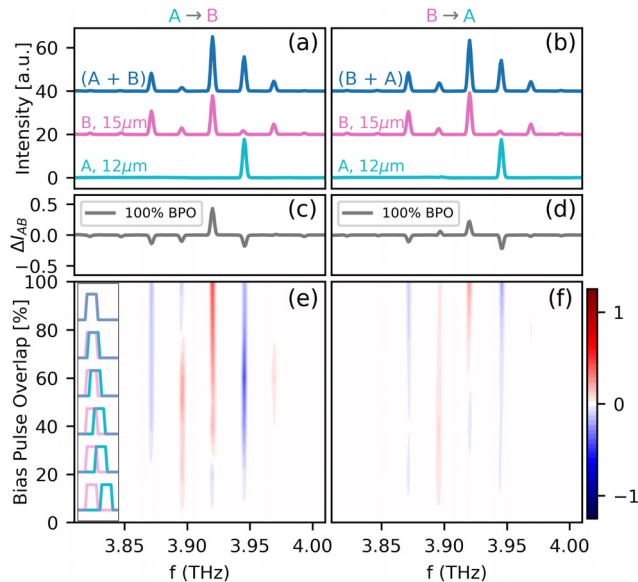
To overcome the asymmetric injection observed in Fig. 2, we characterize a symmetric sample with five uniform 10 μm wide QCWLs. The 10 μm lasers show a reduction of the threshold current density of 50% compared to episide-up devices, enabling continuous-wave operation up to 35 K. In the injection experiments (Fig. 3), we observe the same behavior as for the geometrically dissimilar laser devices. When the bias pulse timing overlaps, the lasers operate in the injection-lock state. They unlock as soon as the bias pulses have a time delay larger than the pulse width.

Additionally, coupling is observed when two ridges that are not direct neighbors are driven in time-synchronized operation. The inset of Fig. 3(f) shows a 2D cross section of the device with the active lasers marked in cyan and pink. Even though the lasers are now spaced more than three free-space wavelengths apart, we still observe injection-locking [Figs. 3(b), 3(d), and 3(f)] with significant changes in the injection-induced differential spectrum.
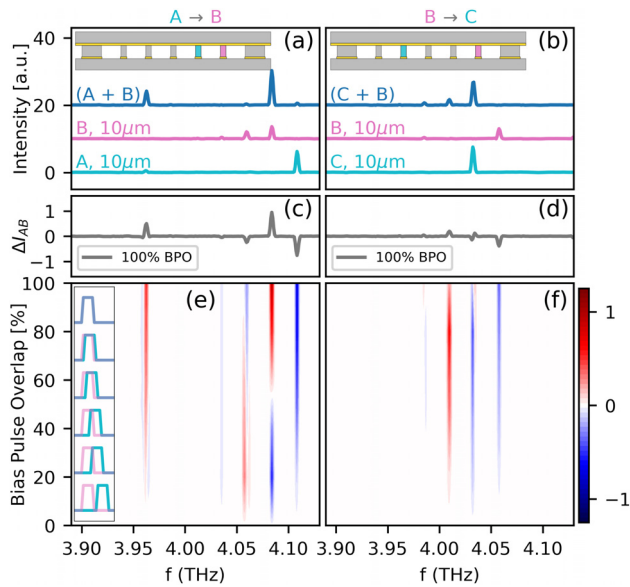
To shed some light on the coupling even over large distances, we performed measurements for six QCWL arrays with different ridge distances [Fig. 4(a)]. The lasers with the smallest spacing of 38 μm ($0.5 * \lambda_0$) show the largest coupling, which decreases exponentially with increasing laser separation as we expect from evanescent field coupling, reaching a minimum around 50 μm separation. Then, it increases again for spacings larger than the free-space wavelength, as the substrate assisted coupling via leaky waves is increasing.

Finite element simulations (see the supplementary material) have been performed to better understand the inter-element coupling mechanisms. Closely spaced QCWLs with separations between 10 and 40 μm couple mostly through their significantly overlapping evanescent field components. For separations larger than 50 μm, laser ridges couple through their common bottom substrate. The leaked radiation is confined within the dielectric-metal waveguide below the laser ridges, enabling efficient coupling even over distances larger than the free space wavelength. The simulation results confirm the distance-dependent measurement results, which show a coupling minimum at 50 μm spacing, visualizing the transition between the two coupling regimes.

Furthermore, intensity dependent measurements on a device with 150 μm ridge spacing show that an increase in the lasing bias of
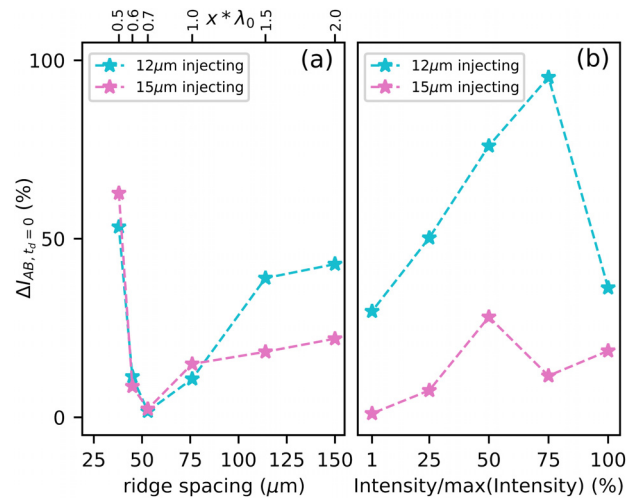
FIG. 3. Spectral evolution of an injection-lock wire laser pair with two 10 μm wide QCWLs. Depicted in (a) are the lasing spectra of the single ridges at device voltages of 22.8 (A) and 23.5 V (B) (cyan and pink, respectively) and the combined spectrum (blue), with the injection-induced differential spectrum ΔI_{AB} at 100% BPO in (c). The contour plot in (e) shows the evolution of the spectral changes with decreasing bias pulse overlap. In this measurement, the lasers are direct neighbors as shown in the inset in (a). The change of the BPO in percent is shown as an inset in (e). (b) The individual and combined spectra of two lasers with more than $3^*\lambda_0$ spacing, with the active lasers depicted in the inset cross section in cyan and pink, with devices voltages 21.1 (C) and 22 V (B). Coupling still occurs even over this large distance, with ΔI_{AB} at 100% BPO depicted in (d) and the corresponding evolution with decreasing BPO in (f). The active lasers are marked in pink and cyan in the inset of (b).

FIG. 4. (a) Distance-dependent measurements of different devices with increasing ridge separation from 38 to 150 μm. Each distance corresponds to a multiple of the free-space wavelength $x * \lambda_0$, visualized by the top x-ticks. The coupling is strong for close-set devices and then attenuates rapidly, as we expect for devices coupling through their evanescent fields. It then increases again for lasers spaced more than one free-space wavelength apart due to substrate assisted coupling. (b) Seed intensity dependent measurements for a 150 μm spaced device at 100% BPO. Depicted are the maximum values of the injection-induced differential spectra ΔI_{AB} at a frequency of 3.93 THz. With increasing lasing intensity of the seeding laser through larger driving bias, the interaction between the ridges increases. Even when biasing the seeding laser at lasing threshold, injection-locking is still observed.

the seeding element increases the mode enhancement. The results are shown in Fig. 4(b). We observe an interaction even when the seeding laser is only biased at lasing threshold. The optimal coupling point may not be at maximum lasing intensity but will differ depending on laser bias, the width of the seeding laser, and the inter-element spacing. In this case, for a device with 150 μm spacing, the maximum interaction is observed at 75% of the maximum intensity of the 12 μm seeding laser and at 50% intensity when the 15 μm laser acts as the seed.

In conclusion, we presented episide-down bonded THz QCWL arrays with individually bias-able elements. The improved thermal properties of these devices lead to a reduction of threshold current densities up to 50%, permitting continuous-wave operation up to 35 K. Simultaneously biased QCWLs injection-lock when the bias pulses of the lasers overlap temporally. This led to a relative intensity enhancement of up to 95% compared to the sum of the intensities of the single spectra. This comparison is possible since each laser ridge can also be biased individually, as the bottom contacts of the die-bonded sample are electrically isolated from each other. Through time delays of the seeding laser's bias pulse, the mode enhancement can be moved to different frequencies. Our symmetric devices demonstrated enhanced coupling strength compared to the asymmetric devices. We demonstrated optical injection-locking over a distance larger than three times the free-space wavelength between the locked pair. From the study of

the spacing dependence on the coupling strength, we find that the lasers couple not only through the evanescent field but also through the "substrate waveguide" formed as part of the die-bonding process. Coupling was also improved by reducing the lasing intensity of the seeding laser, which led to an increasing exhaustion of the provided gain range.

With the advancements demonstrated in this work, the next steps could involve integrating mode selection into the simple Fabry–Pérot ridge waveguides, in the form of distributed feedback gratings. This will enable better control of the emission properties and ensure proper overlap of the paired lasers' spectra. Using a different active material better optimized for low threshold currents may allow us to bias even more devices simultaneously. Finally, the utilized die-bonding technique enables many more applications like designing multicolored THz sources by combining different active materials on the same substrate, integrating the injection-lock QCWLs on chips with other optical components and enabling the creation of photonic circuits and lab-on-a-chip set-ups.

See the supplementary material for pulsed and continuous-wave measurements of the power and voltage vs current (PIV) characteristics of the wire lasers and finite element simulation results.

AUTHOR DECLARATIONS

Conflict of Interest

The authors have no conflicts to disclose.

Author Contributions

Marie C. Ertl: Conceptualization (lead); Data curation (lead); Formal analysis (lead); Investigation (lead); Methodology (lead); Visualization (lead); Writing – original draft (lead). **Michael Jaidl:** Conceptualization (supporting); Investigation (supporting); Methodology (supporting); Writing – review & editing (supporting). **Benedikt Limbacher:** Investigation (supporting); Methodology (supporting). **Dominik Theiner:** Investigation (supporting); Methodology (supporting). **Miriam Giparakis:** Investigation (supporting); Methodology (supporting); Writing – review & editing (supporting). **Stefania Isceri:** Methodology (supporting). **Maximilian Beiser:** Methodology (supporting). **Aaron Maxwell Andrews:** Methodology (supporting); Resources (supporting); Writing – review & editing (supporting). **Gottfried Strasser:** Resources (supporting). **Juraj Darmo:** Conceptualization (supporting); Data curation (supporting); Formal analysis (supporting); Investigation (supporting); Methodology (supporting); Supervision (supporting); Validation (supporting); Writing – review & editing (supporting). **Karl Unterrainer:** Conceptualization (supporting); Data curation (supporting); Funding acquisition (lead); Investigation (supporting); Methodology (supporting); Project administration (lead); Resources (equal); Supervision (lead); Validation (lead); Writing – review & editing (lead).

DATA AVAILABILITY

The data that support the findings of this study are available from the corresponding author upon reasonable request.

REFERENCES

[1]J. Zhang, D. Chu, S. Wu, S.-T. Ho, W. Bi, C. Tu, and R. Tiberio, "Photonic-wire laser," Phys. Rev. Lett. **75**, 2678 (1995).

[2]E. Orlova, J. Hovenier, T. Klaassen, I. Kašalynas, A. Adam, J. Gao, T. Klapwijk, B. Williams, S. Kumar, Q. Hu *et al.*, "Antenna model for wire lasers," Phys. Rev. Lett. **96**, 173904 (2006).

[3]M. I. Amanti, G. Scalari, F. Castellano, M. Beck, and J. Faist, "Low divergence terahertz photonic-wire laser," Opt. Express **18**, 6390–6395 (2010).

[4]E. Orlova, J. Hovenier, P. De Visser, and J. Gao, "Image beam from a wire laser," Phys. Rev. A **91**, 051802 (2015).

[5]A. Khalatpour, J. L. Reno, N. P. Kherani, and Q. Hu, "Unidirectional photonic wire laser," Nat. Photonics **11**, 555–559 (2017).

[6]S. Biasco, K. Garrasi, F. Castellano, L. Li, H. E. Beere, D. A. Ritchie, E. H. Linfield, A. G. Davies, and M. S. Vitiello, "Continuous-wave highly-efficient low-divergence terahertz wire lasers," Nat. Commun. **9**, 1122 (2018).

[7]B. S. Williams, "Terahertz quantum-cascade lasers," Nat. Photonics **1**, 517–525 (2007).

[8]Z. Zhou, T. Zhou, S. Zhang, Z. Shi, Y. Chen, X. Wan, X. Li, X. Chen, S. N. Gilbert Corder, Z. Fu *et al.*, "Multicolor t-ray imaging using multispectral metamaterials," Adv. Sci. **5**, 1700982 (2018).

[9]A. Goyal, T. Myers, C. A. Wang, M. Kelly, B. Tyrrell, B. Gokden, A. Sanchez, G. Turner, and F. Capasso, "Active hyperspectral imaging using a quantum cascade laser (QCL) array and digital-pixel focal plane array (DFPA) camera," Opt. Express **22**, 14392–14401 (2014).

[10]P. Rauter, S. Menzel, A. K. Goyal, C. A. Wang, A. Sanchez, G. Turner, and F. Capasso, "High-power arrays of quantum cascade laser master-oscillator power-amplifiers," Opt. Express **21**, 4518–4530 (2013).

[11]Q. Qin, B. S. Williams, S. Kumar, J. L. Reno, and Q. Hu, "Tuning a terahertz wire laser," Nat. Photonics **3**, 732–737 (2009).

[12]Q. Qin, J. L. Reno, and Q. Hu, "MEMS-based tunable terahertz wire-laser over 330 GHz," Opt. Lett. **36**, 692–694 (2011).

[13]N. Han, A. de Geofroy, D. P. Burghoff, C. W. I. Chan, A. W. M. Lee, J. L. Reno, and Q. Hu, "Broadband all-electronically tunable MEMS terahertz quantum cascade lasers," Opt. Lett. **39**, 3480–3483 (2014).

[14]Q. Qin, N. Han, T.-Y. Kao, J. L. Reno, and Q. Hu, "Effective mode selector for tunable terahertz wire lasers," Opt. Lett. **38**, 407–409 (2013).

[15]T.-Y. Kao, X. Cai, A. W. Lee, J. L. Reno, and Q. Hu, "Antenna coupled photonic wire lasers," Opt. Express **23**, 17091–17100 (2015).

[16]A. Khalatpour, J. L. Reno, and Q. Hu, "Phase-locked photonic wire lasers by π coupling," Nat. Photonics **13**, 47–53 (2019).

[17]T.-Y. Kao, J. L. Reno, and Q. Hu, "Phase-locked laser arrays through global antenna mutual coupling," Nat. Photonics **10**, 541–546 (2016).

[18]M. Krall, M. Brandstetter, C. Deutsch, H. Detz, A. M. Andrews, W. Schrenk, G. Strasser, and K. Unterrainer, "Subwavelength micropillar array terahertz lasers," Opt. Express **22**, 274–282 (2014).

[19]U. Senica, A. Forrer, T. Olariu, P. Micheletti, S. Cibella, G. Torrioli, M. Beck, J. Faist, and G. Scalari, "Planarized THz quantum cascade lasers for broadband coherent photonics," Light Sci. Appl. **11**, 347 (2022).

[20]P. Micheletti, U. Senica, A. Forrer, S. Cibella, G. Torrioli, M. Frankié, M. Beck, J. Faist, and G. Scalari, "Terahertz optical solitons from dispersion-compensated antenna-coupled planarized ring quantum cascade lasers," Sci. Adv. **9**, eadf9426 (2023).

[21]J. Katz, S. Margalit, and A. Yariv, "Diffraction coupled phase-locked semiconductor laser array," Appl. Phys. Lett. **42**, 554–556 (1983).

[22]W. Streifer, D. Welch, P. Cross, and D. Scifres, "Y-junction semiconductor laser arrays: Part I—Theory," IEEE J. Quantum Electron. **23**, 744–751 (1987).

[23]L. K. Hoffmann, C. Hurni, S. Schartner, M. Austerer, E. Mujagić, M. Nobile, A. Benz, W. Schrenk, A. M. Andrews, P. Klang *et al.*, "Coherence in y-coupled quantum cascade lasers," Appl. Phys. Lett. **91**, 161106 (2007).

[24]D. Botez and G. Peterson, "Modes of phase-locked diode-laser arrays of closely spaced antiguides," Electron. Lett. **24**, 1042–1044 (1988).

[25]M. Rösch, G. Scalari, G. Villares, L. Bosco, M. Beck, and J. Faist, "On-chip, self-detected terahertz dual-comb source," Appl. Phys. Lett. **108**, 171104 (2016).

[26]D. Ackley, "Single longitudinal mode operation of high power multiple-stripe injection lasers," Appl. Phys. Lett. **42**, 152–154 (1983).

[27]M. Jaidl, N. Opačak, M. Kainz, D. Theiner, B. Limbacher, M. Beiser, M. Giparakis, A. Andrews, G. Strasser, B. Schwarz *et al.*, "Silicon integrated terahertz quantum cascade ring laser frequency comb," Appl. Phys. Lett. **120**, 091106 (2022).

[28]M. A. Kainz, S. Schönhuber, B. Limbacher, A. M. Andrews, H. Detz, G. Strasser, G. Bastard, and K. Unterrainer, "Color switching of a terahertz quantum cascade laser," Appl. Phys. Lett. **114**, 191104 (2019).

23 September 2024 07:57:55